DOI: 10.15480/882.9306

Eighth International Symposium on Marine Propulsors
smp'24, Berlin, Germany, March 2024

Numerical Simulation of Uniform Inflow Propeller Noise Based on Acoustic Analogy Method

Zhai Shu-cheng[1,2], Xiong Zi-ying[1,2], Hong Fang-wen[1,2]

[1] China Ship Scientific Research Center, Wuxi, China
[2] Taihu Laboratory of Deepsea Technological Science, Wuxi, China

ABSTRACT

The underwater radiated noise of the propeller was studied in this paper using a CFD method in combination with the acoustic analogy equation. The loading noise excited by the turbulent pulsation pressure and the thickness noise caused by the rotational motion of the propeller were obtained by the LES method. Then, the propeller noise was predicted using the Formulation 1A integral formula. The boundary layer characteristics of the blade surface were analyzed, and the characteristics of wall fluctuating pressure were extracted and analyzed. Due to the existence of pressure gradients on the suction surface and the pressure surface, it is difficult to obtain uniform pulsating pressure dimensionless results by using the internal or external parameters of the boundary layer, and this feature is more obvious at the 0.7R radius of the blade. Finally, the acoustic analogy method was used to predict the propeller noise. The 1.25 kHz frequency band was in good agreement with the experimental results. Through the analysis of thickness noise and loading noise source characteristics, the noise of the blade generated in this frequency band mainly came from the loading noise. The results can serve as a technical guide for the investigation of propeller underwater radiated noise.

Keywords

Propeller noise, CFD, FW-H, Acoustic analogy method, Fluctuating pressure.

1 INTRODUCTION

Both direct and indirect methods can be used to solve the sound propagation problem. The direct method mainly solves the compressible Navier-Stokes equation to obtain sound pressure pulsation. Due to the huge difference between the magnitude of sound pressure and the fluid density, a high-order discrete scheme with low dissipation and low frequency dispersion should be adopted in the solution process (Bogey et al 2004). However, it is difficult to solve the sound field at high Reynolds number, especially the far-field radiated sound. The other method mainly uses the mixed method to solve the problem of sound propagation. Its idea is to solve the near-field sound source term first, and then solve the far-field sound radiation problem by the method of acoustic analogy. The acoustic analogy method is mainly used for the prediction of the sound field of non-reflected radiation, and it is the simplest method in dealing with the far-field acoustic radiation, so it is widely used.

Since the 1950s, when Lighthill proposed the Lighthill equation (Lighthill 1952), acoustic analogy method has gradually developed by Curle (1955), Ffowcs Williams and Hawkings (1969). Ffowcs Williams-Hawkings (FW-H) equation, which can consider the acoustic radiation of moving sound sources, has become a hot topic in the study of acoustic radiation. However, the use of the FW-H equation also has its own limitations. For example, when the rotation speed to be studied approaches the speed of sound, the quadrupole term of the FW-H equation needs to be considered, and the sound source term needs to be dealt with in the way of a volume integral, which makes the processing of the FW-H equation more complicated. Brentner et al (1998) adopted the collapse sphere model to simplify the solution of the quadrupole term, and gave the integral formula of the quadrupole sound source, but this model needs a large amount of integral data and calculation. Francescantonio (1997) noted that Kirchhoff equation uses a virtual surface wrapped with a sound source as the integral surface when solving the wave equation, and developed the Kirchhoff FW-H (KFW-H) method, which has higher computational efficiency than the FW-H equation because it does not need volume integration. However, the KFW-H integral surface needs to be selected in the linear sound source region. When there is wake flow across the integral surface, pseudo noise will be generated due to the influence of truncation error, such

as propeller wake flow. To solve this problem, Nitzkorski (2015) proposed a so-called dynamic end caps method for integral surface processing. The flux generated by the velocity term corresponding to the quadrupole sound source at the multiple end faces was modified to the integral surface of the FW-H equation, which was verified in the flat plate noise at the trailing edge of the blunt body. For the prediction of underwater propeller radiated noise, firstly it is necessary to obtain the sound source information, then use the FW-H equation to predict the propeller far-field radiated sound. Different flow field solving methods can be chosen for different frequency bands of solving noise. For example, when the low-frequency tone spectrum information of the propeller is of primary interest, the RANS method can be used, as shown by Lloyd et al (2014), S. Ianniello et al (2013), Hallander et al (2012), Jang et al (2015), while high-precision LES method or DES methods can be used for the medium and high frequency information also the broadband noise information of propeller, such as Bensow et al (2016), Lidtke et al (2016), Cianferra et al (2019), etc. In general, the flow Reynolds number on the blade surface of the propeller in the model state is between 10^5 and 10^6, and the real-time solution of the pulsating pressure on the blade surface is a turbulent boundary layer flow question, so it is difficult to obtain the sound source term of the pulsating pressure with high temporal and spatial precision. The FW-H method also has some limitations, for example, it cannot solve the acoustic reflection problem, such as the far-field acoustic radiation problem of propeller with a duct. In this case, the acoustic boundary element method can be used (Seol et al 2002). Due to the complexity of underwater propeller radiation noise, the numerical solution of a flow field based on the acoustic analogy method needs to be firstly solved by a CFD method. Although the Mach number in water is low and the quadrupole sound source with nonlinear term can be ignored, the solution of dipole sound source is still full of challenges.

2 NUMERICAL METHOD

2.1 Large Eddy Simulation

Using the filter function to filter the incompressible Navier-Stokes equation, the following equation can be obtained:

$$\frac{\partial \bar{u}_i}{\partial x_i} = 0$$
$$\frac{\partial}{\partial t}(\rho \bar{u}_i) + \frac{\partial}{\partial x_j}(\rho \bar{u}_i \bar{u}_j) = \frac{\partial}{\partial x_j}\left(\mu \frac{\partial \bar{u}_i}{\partial x_j}\right) - \frac{\partial \bar{p}}{\partial x_i} - \frac{\partial \tau_{ij}}{\partial x_j} \quad (1)$$

Where: $\tau_{ij} = \rho\overline{u_i u_j} - \rho \bar{u}_i \bar{u}_j$ is the Sub-grid Stress Tensor, which is the momentum transport of filtered small scale pulsation and large scale pulsation. The form of sub-grid stress is similar to Reynolds stress. For the unclosed term at the right end of the governing equation, a sub-grid stress model must be constructed to seal it. Similar to Reynolds stress, the sub-grid stress tensor is established with reference to the Boussinesq hypothesis as follows:

$$\tau_{ij} = \frac{1}{3}\tau_{kk}\delta_{ij} - 2\mu_t \bar{S}_{ij} \quad (2)$$

μ_t is the sub-grid turbulent viscosity, and $\bar{S}_{ij}$ is the second order tensor of strain stress. For sub-grid turbulent viscosity, this paper uses the advanced Wall-Adapting Local-EddyViscosity (WALE) model (Nicoud et al 1999). Compared with the Smagorinsky's sub-grid model, the wall damping function is not required, and the empirical parameters are not sensitive to the calculation results. In the WALE model, vorticity viscosity is expressed as:

$$\mu_t = \rho L_s^2 \frac{\left(S_{ij}^d S_{ij}^d\right)^{3/2}}{\left(\bar{S}_{ij}\bar{S}_{ij}\right)^{5/2} + \left(S_{ij}^d S_{ij}^d\right)^{5/4}} \quad (3)$$

Where L_s and S_{ij}^d are defined in the WALE model as follows:

$$L_s = \min\left(kd,\ C_w V^{1/3}\right) \quad (4)$$

$$S_{ij}^d = \frac{1}{2}\left(\bar{g}_{ij}^2 + \bar{g}_{ji}^2\right) - \frac{1}{3}\delta_{ij}\bar{g}_{kk}^2,\ \ \bar{g}_{ij} = \frac{\partial \bar{u}_i}{\partial x_j} \quad (5)$$

Where: k is the Karman constant and the value is 0.41; d is the distance from the wall; V is the mesh volume; C_w is the empirical parameter and the value is 0.544.

2.2 Acoustic Analogy Method

FW-H equation is a non-homogeneous wave equation, which is derived from continuity equation and momentum equation. Its expression is as follows:

$$\begin{aligned} \frac{1}{c_0^2}\frac{\partial^2 p'}{\partial t^2} - \nabla^2 p' &= \frac{\partial^2}{\partial x_i \partial x_j}[T_{ij}H(f)] \\ &\quad - \frac{\partial}{\partial x_i}\left[L_{ij}n_j\delta(f)\right] \\ &\quad + \frac{\partial}{\partial t}\{\rho_0 U_n \delta(f)\} \\ L_{ij} &= P_{ij} + \rho u_i(u_n - v_n) \\ U_i &= u_i + (\tfrac{\rho}{\rho_0} - 1)(u_n - v_n) \end{aligned} \quad (6)$$

where u_i is the fluid velocity in the direction of x_i, u_n is the normal fluid velocity of the control surface $f = 0$, v_n is the normal velocity of the control surface element, v_i is the velocity in x_i direction of the control surface element, $\delta(f)$ is the Dirac delta function, taking 1 only on the integral surface f and 0 elsewhere, $H(f)$ is the Heaviside function, with H=1 if f >0, H=0 if f <0. p' is the sound pressure of the far field $p' = p - p_0$. For the above equation, f =0 is the control surface of the sound source embedded in the unbounded flow field, which can be an impermeable surface (impenetrable to the fluid) or a permeable surface including the object (a certain distance from the object surface, the fluid can cross). When u_n=v_n, Equation (6) can be used to describe the case of an impenetrable surface of the sound source. It should be noted that when the permeable surface sound source is used, due to the certain distance between the integral surface and the object surface, this part of the fluid needs to be solved fine. n_i is the unit normal vector (f >0 is

positive), c_0 is the far-field sound velocity, T_{ij} is Lighthill stress tensor, defined as:

$$T_{ij} = \rho v_i v_j + P_{ij} - c_0^2(\rho - \rho_0)\delta_{ij} \quad (7)$$

P_{ij} is the compressive stress tensor, which for incompressible flows can be defined as:

$$P_{ij} = p\delta_{ij} - \mu\left[\frac{\partial u_i}{\partial x_j} + \frac{\partial u_j}{\partial x_i} - \frac{2}{3}\frac{\partial u_k}{\partial x_k}\delta_{ij}\right] \quad (8)$$

FW-H equation can easily classify sound sources, which brings great convenience to the study of noise. It divides sound sources into monopole sound sources, dipole sound sources and quadrupole sound sources. When the radiated acoustic observation point is located at x, if the generalized function and free space Green's function are used to solve Equation (6), the integral solution of FW-H equation can be obtained as follows:

$$p'(x,t) = p'_T(x,t) + p'_L(x,t) + p'_Q(x,t) \quad (9)$$

The monopole term:

$$4\pi p'_T(x,t) = \int_{f=0}\left[\frac{\rho_0(U_n + \dot{U}_n)}{r(1-M_r)^2}\right]_{ret}dS + \int_{f=0}\left[\frac{\rho_0 U_n(r\dot{M}_r + c_0(M_r - M^2))}{r^2(1-M_r)^3}\right]_{ret}dS \quad (10)$$

The dipole term:

$$4\pi p'_L(x,t) = \frac{1}{c_0}\int_{f=0}\left[\frac{\dot{L}_r}{r(1-M_r)^2}\right]_{ret}dS + \int_{f=0}\left[\frac{L_r - L_M}{r^2(1-M_r)^2}\right]_{ret}dS + \frac{1}{c_0}\int_{f=0}\left[\frac{L_r(r\dot{M}_r + c(M_r - M^2))}{r^2(1-M_r)^3}\right]_{ret}dS \quad (11)$$

Where: $U_i = v_i + \frac{\rho}{\rho_0}(u_i - v_i)$, $L_i = P_{ij}\hat{n}_j + \rho u_i(u_n - v_n)$, $M_i = U_i/c_0$.

The radiation efficiency of the quadrupole sound source is the fifth power of the Mach number, the dipole is the third power, and the Mach number in water is usually less than 0.1, so that the radiation efficiency of the quadrupole sound source is low and can be ignored. The above Equation (9), (10) and (11) are the Formulation 1A integral formula, which mainly solves the delay problem between the source and the observer, and the subscript ret represents the time delay τ. If the observer's time is t and the distance between the observer and the source is r, then $\tau = t - \frac{r}{c_0}$. When the integral surface of the sound source is an impenetrable object surface, $p'_T(x,t)$ is called the thickness sound source term, which is mainly caused by the movement of objects in the flow field to displace the fluid, such as the noise caused by blade rotation. $p'_L(x,t)$ is called the loading sound source term, which is mainly generated by the distributed force source on the surface of the object in the flow field, such as the pulsating pressure on the surface of the blade. The thickness sound source and the loading sound source are collectively referred to as the surface sound source term, while the quadrupole sound source term $p'_Q(x,t)$ is generated by the nonlinear term of the main fluid (such as turbulent stress, etc.), which requires the volume integral of the sound source. When the Mach number is high, the contribution of this sound source to the radiated sound increases. Due to the low Mach number of the rotating propeller in water, the quadrupole sound source can be ignored.

The sound pressure pulsation at the receiving point of the sound source can be obtained from the Formulation 1A integral formula, then, the sound pressure information in the frequency domain can be obtained by fast Fourier transform, and expressed by the method of sound pressure level:

$$L_p(f_i) = 20\log\frac{p(f_i)}{p_{ref}} \quad (12)$$

Where: p_{ref}=10^{-6} Pa; f_i is the center frequency of 1/3 Oct, subscript i is the i-th frequency point, Hz; $p(f_i)$ is the sound pressure at f_i, Pa; $L_p(f_i)$ is the sound pressure spectrum level at 1/3 Oct center frequency, dB.

3 RESEARCH OBJECT AND GRID GENERATION

3.1 Model

The model is a four-blade fixed-pitch propeller, and the main parameters are shown in Table 1. This propeller is a scaled model for ordinary merchant ships with a disk area ratio of 0.4. The 3D propeller model is shown in Figure 1. The propeller blade is made of aluminum alloy.

Table 1 Main parameters of propeller

Items	Symbol	Value
Diameter	D/mm	240
Disk ratio	A_e/A_o/-	0.40
Pitch ratio	$(P/D)_{0.7R}$/-	0.7901
Profile	naca	naca66-mod
Number of blades	Z/-	4
Rotation	/	Right hand

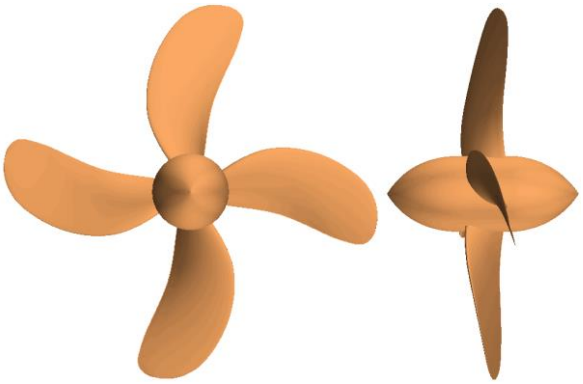

Figure 1 Geometry of the propeller

3.2 Mesh

An unstructured cell is used to resolve the whole domain, the maximum cell of propeller surface is 0.5%D, and the

minimum cell scale is 0.02%D, and the boundary layer is divided by prismatic cell. The number of boundary layers is 10 with an increase ratio of 1.2, and the total number of cells is about 45 million. For the comparative study, the number of coarse cells is 11.2 million. At this time, the maximum and minimum values of the propeller surface mesh are 1%D and 0.04%D, respectively. The propeller surface cell and boundary layer cell are shown in Figure 2. The calculation domain is cylindrical, in which the entrance distance is 5D from the blade, the exit distance is 10D from the blade, the radius of the cylinder is 5D, and the rotating area of the propeller is a cylinder with a diameter of 1.1D, as shown in Figure 5. The velocity flow boundary condition is adopted at the entrance, the pressure outlet boundary condition is adopted at the exit. At the inlet, the method of synthetic vortex is used to give the turbulent state of the inlet, and the number of initialized vortices is 1000 (Jarrin et al 2006). The propeller rotation is simulated by sliding mesh method, and the data exchange between the moving region and the stationary region is transmitted by interface mode. The calculation interval is 5E-05s, and the total time length is 1.1s. Figure 3 shows the wall y^+ on propeller surface. The main areas are lower than 2, which means that the first cell layer on the propeller surface reaches the viscous sublayer.

(a) Cells around the blades

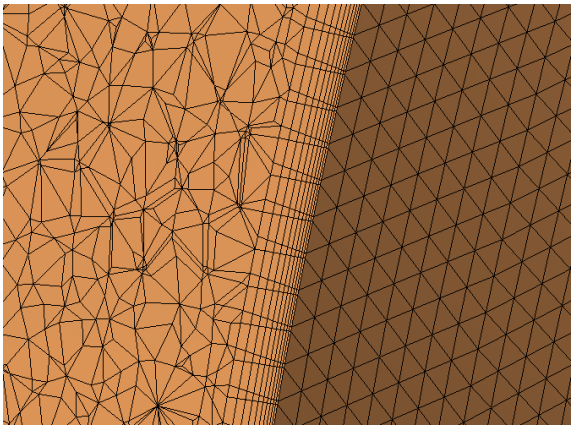

(b) Boundary layer of the blade surface

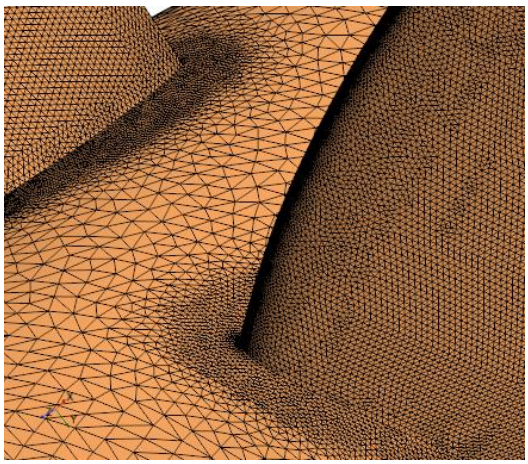

(c) Cells at the leading edge

Figure 2 Cell snapshot

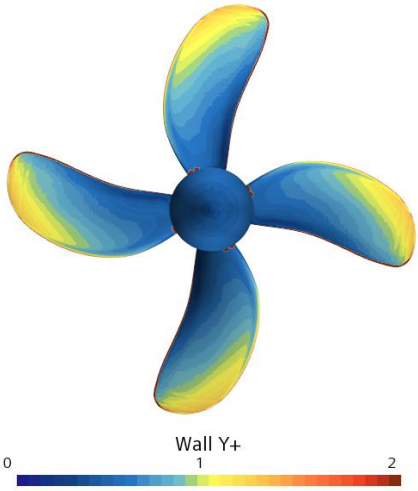

Figure 3 Wall Y+ of the propeller

4 RESULT ANALYSIS

4.1 Hydrodynamic Performance

The open water performance is shown in Figure 4. The advance coefficient is defined as $J = U/nD$ and the propeller design point is J=0.556, and the hydrodynamic and noise performance of the propeller at the design point are analyzed in the noise calculation process.

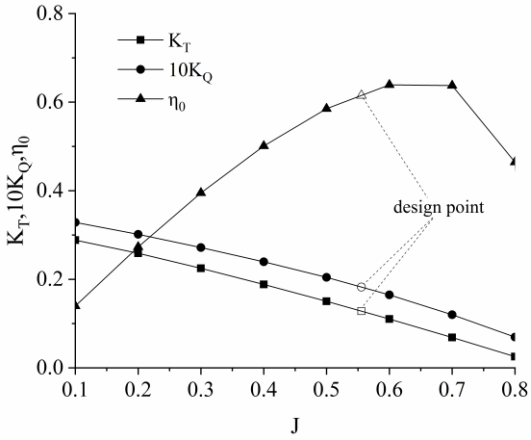

Figure 4 Open water performance (CFD)

4.2 Boundary Layer Characteristics

Firstly, the characteristics of the mean flow field are analyzed. The airfoil with arch is generally used for the propeller blade profile, and the pressure gradient exists on the surface of the airfoil. The pressure coefficient on the surface of the propeller blade is shown in Figure 6, where the distribution of the average pressure coefficient of different radii is extracted, as shown in Figure 7. The variation of the pressure gradient can be evaluated via Equation (13). Figure 8 shows the distribution of pressure gradient coefficient β. Due to the drastic change of pressure gradient at the nose and trailing edge of the profile, the β value changes greatly, while in the middle region, the β value changes little. It can be seen that the pressure surface has wider coverage than the suction surface with zero pressure gradient. For example, at 0.5R and 0.7R radius in the range of x/C=0.1~0.8, β is almost zero, but there is almost no zero pressure gradient distribution at 0.9R. In addition, there is almost no zero pressure gradient distribution area on the suction surface of the blade.

$$\beta = \frac{\delta^*}{\tau_w}\frac{\partial p}{\partial x} \tag{13}$$

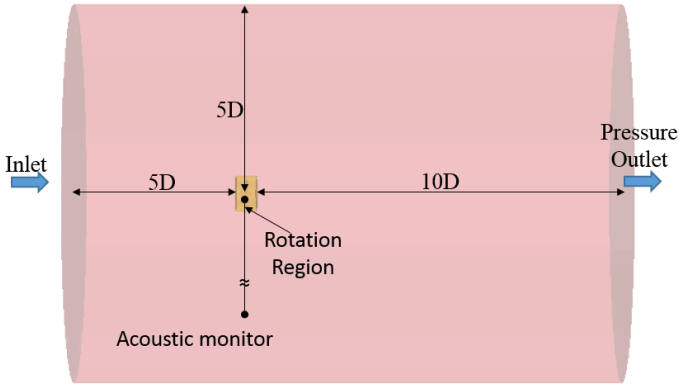

Figure 5 Computation domain and acoustic monitor

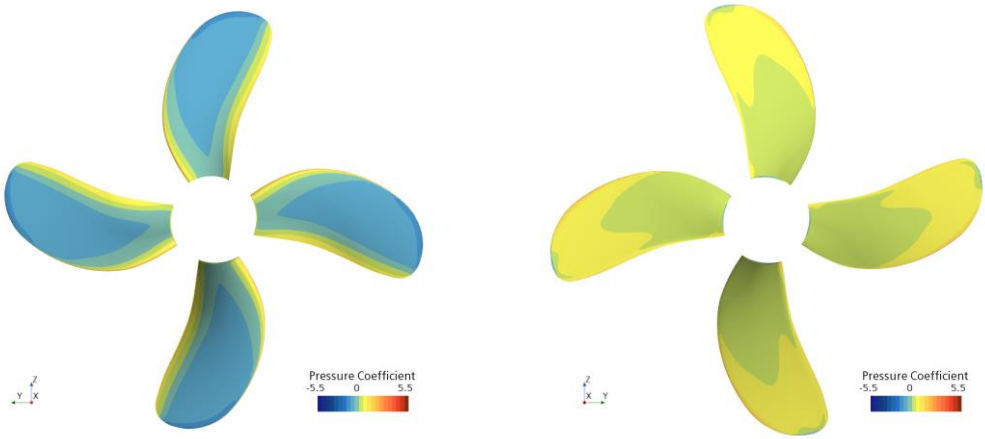

(a) (b)

Figure 6 Pressure distribution on the blade surface, (a) suction side, (b) pressure side

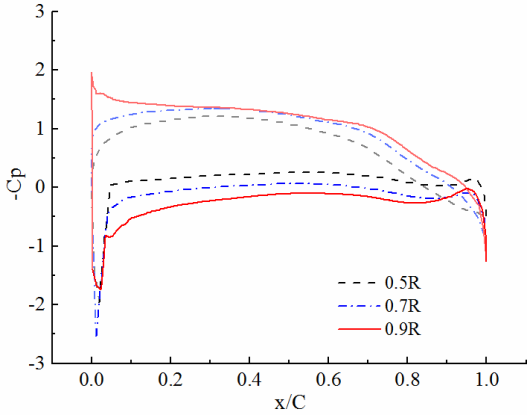

Figure 7 Pressure distribution on blade profiles

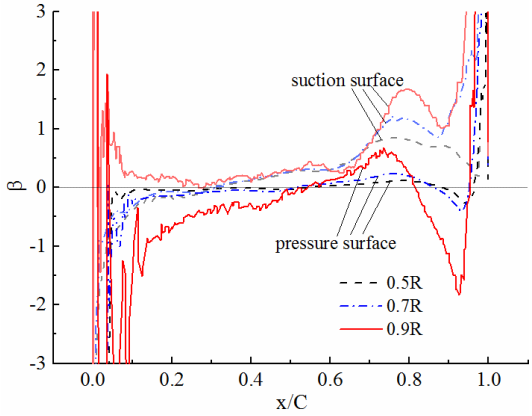

Figure 8 Pressure gradient distribution on blade profiles

The characteristics of the boundary layer on the blade surface are extracted and analyzed. The boundary is usually defined as the position where the normal extension along the wall reaches 99% of the incoming flow velocity and is represented by the symbol δ. Due to the velocity pulsation in the real boundary layer, this definition is a difficult quantity to determine and has certain a arbitrariness. Generally speaking, more accurate integrated quantities are used to determine boundary layer parameters. Such as the displacement thickness and momentum loss thickness:

$$\delta^*(x) = \int_0^\infty (1 - \frac{U}{U_0})dy \tag{14}$$

$$\theta(x) = \int_0^\infty \frac{U}{U_0}(1 - \frac{U}{U_0})dy \tag{15}$$

Where U is the velocity distribution parallel to the wall, and U_0 is the incoming flow velocity. The momentum loss thickness represents the momentum loss of the fluid in the boundary layer, reflecting the resistance of the object in the fluid, and the momentum loss Reynolds number is defined as $Re_\theta = U\theta/v$. Wall shear stress and wall friction velocity are defined as follows:

$$\tau_w = \rho v(\frac{dU}{dy})_{y=0} \tag{16}$$

$$u_\tau = \sqrt{\tau_w/\rho} \tag{17}$$

Figure 9 shows the velocity profile of the boundary layer, and gives the velocity distribution of different radius and different chord length positions respectively. At the radius of 0.5R, the velocity at the positions of 0.25C and 0.5C, both the blade surface and the back of the blade, are well satisfying the logarithmic law, but at the position of 0.75C is slightly deviated, possibly because there is a flow separation phenomenon here, which affects the velocity distribution law. At the 0.7R radius blade surface, the range of the logarithmic law region is smaller than that at the back of the blade, because the pressure gradient on the suction surface is larger, while most of the pressure surface has zero pressure gradient. The logarithmic law region of the 0.9R radius is narrower at 0.25C and increases significantly along the chord length, such as at 0.5C and 0.75C. Figure 10 shows the changes of boundary layer parameters on the blade surface. In general, with the increase of radius, boundary layer thickness, displacement thickness, momentum thickness and friction velocity decrease, while the suction surface is higher than the pressure surface. With the same radius, most parameters increase along the blade profile, except the friction velocity.

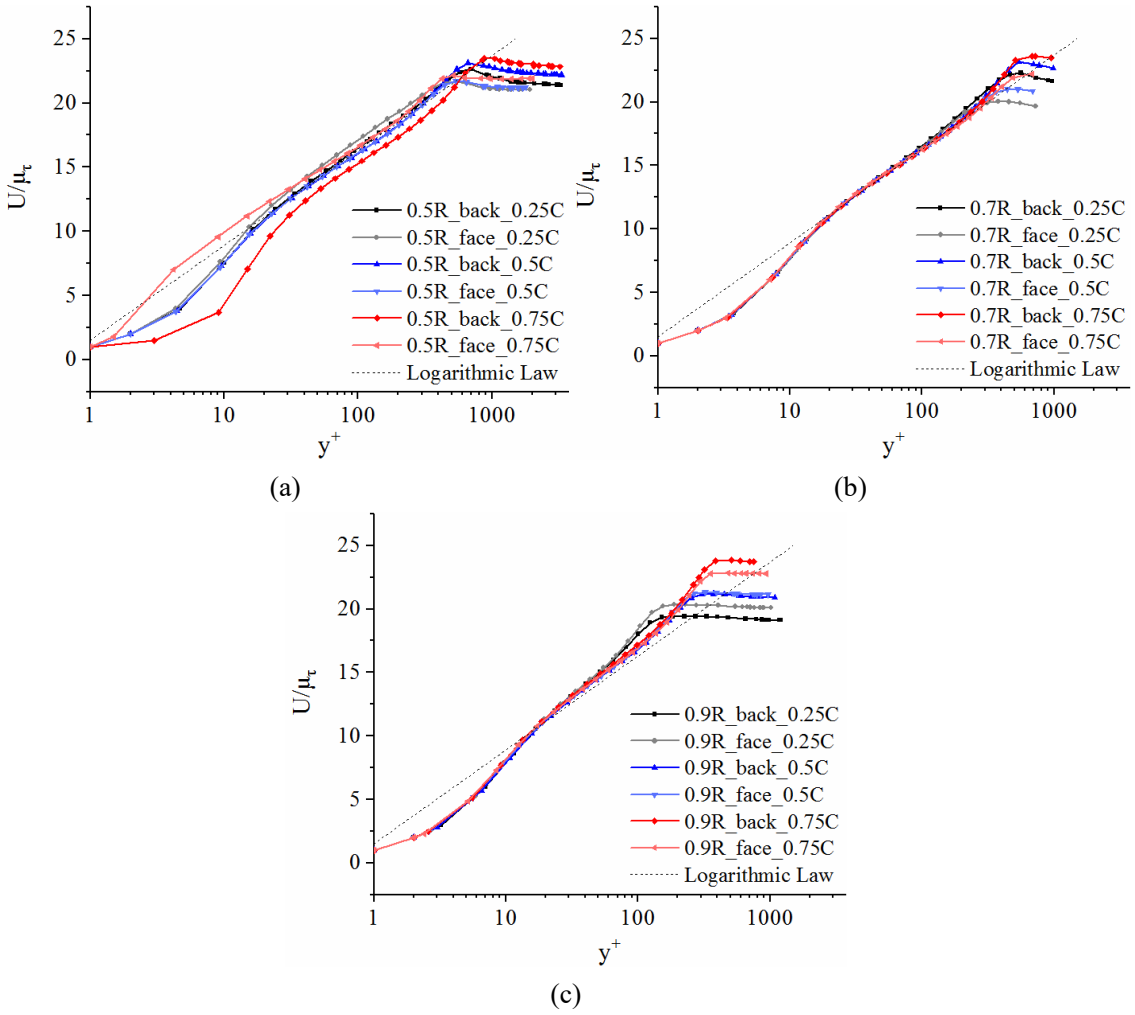

Figure 9 Boundary layer velocity profile, (a) different chord length positions at 0.5R, (b) different chord length positions at

0.7R, (c) different chord length positions at 0.9R

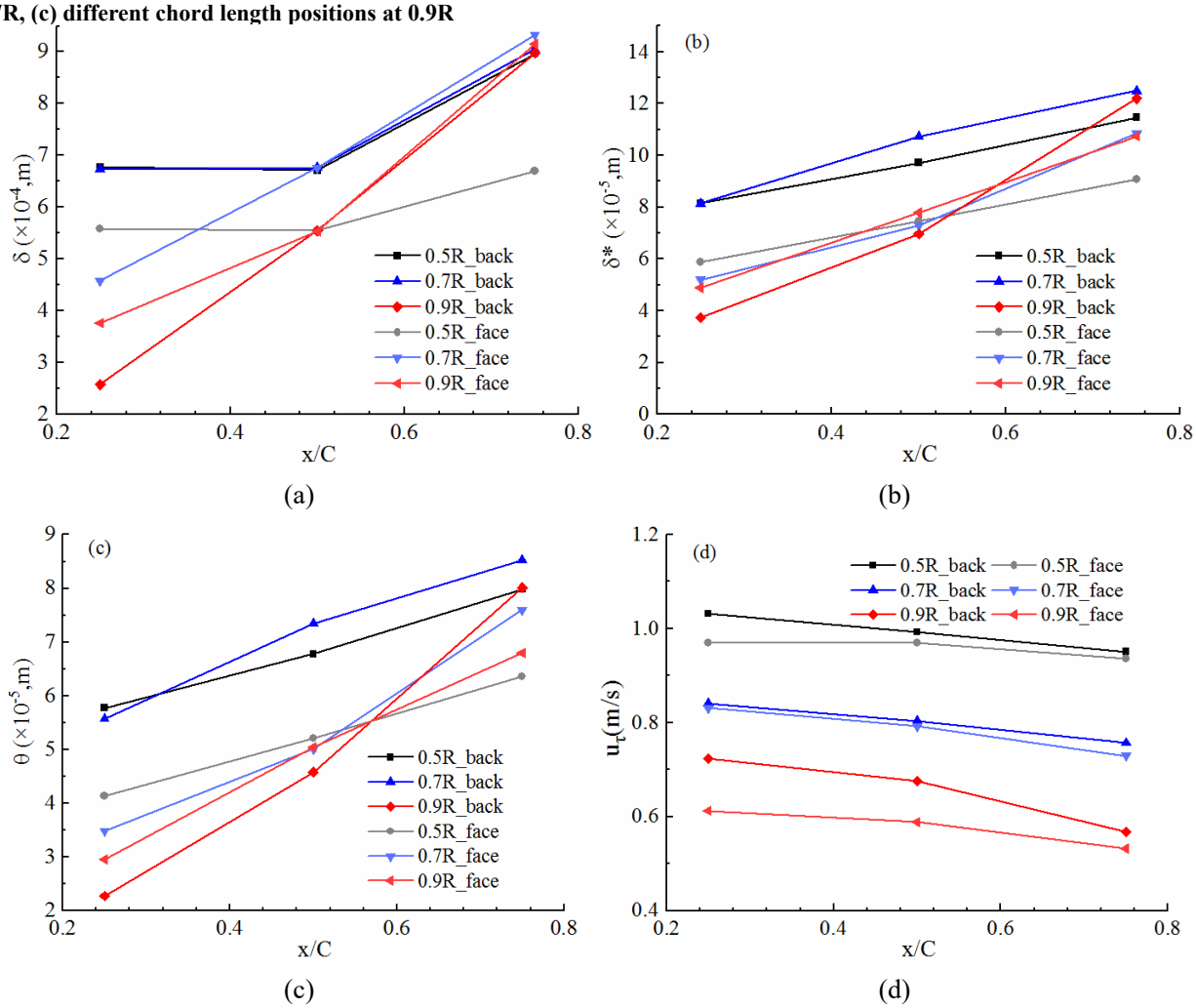

Figure 10 Boundary layer parameter, (a) boundary layer thickness, (b) displacement thickness, (c) momentum loss thickness, (d) friction velocity

4.3 Wall Fluctuating Pressure Characteristics

The time signal of pressure pulsation on the blade surface is extracted, and the root mean square of pressure pulsation is analyzed, as shown in Figure 11, where $\mathrm{Re}_\tau = \mu_\tau \delta / \upsilon$. Farabee and Casarella (1991) give the curve of pressure pulsation of the zero pressure gradient plate flow with an empirical formula. At the radius of 0.7R and 0.5R, the pressure gradient is close to the condition of zero pressure gradient, so the agreement is relatively good, but there is a large pressure gradient at the position of 0.9R, the dispersion is relatively large. Magionesi (2016) gives the test results, but when there is a pressure gradient, the test results also have a certain dispersion deviation from the empirical formula.

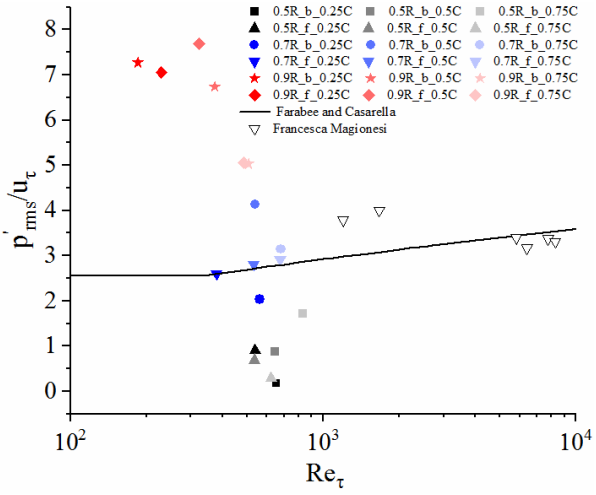

Figure 11 The blade surface pulsating pressure varies with Reynolds number

The spectrum of wall pulsating pressure is expressed as:

$$\phi(\omega) = \frac{1}{2\pi}\int_{-\infty}^{\infty} C_{pp}(\tau) e^{-i\omega\tau} d\tau \qquad (18)$$

C_{pp} is the pulsating pressure autocorrelation function, and the boundary layer parameters in Figure 10 are used for dimensionless treatment. δ / u_τ is used for the outer

boundary layer parameters, and $\nu/u_\tau{}^2$ is used for the inner boundary layer parameters. The mainstream view is that the low-frequency part of turbulent pulsating pressure is mainly due to the large-scale vortex excitation of turbulence, which mainly concentrates in the outer region of the turbulent boundary layer, while the inner region mainly concentrates small-scale vortices, and the high-frequency characteristics of turbulent pulsating pressure stimulated by small-scale vortices. Figure 12 shows the dimensionless processing results with the outer parameters of the turbulent pulsation pressure spectrum. It can be seen that the low frequency band at 0.9R has better normalization effect, while the low frequency band at 0.5R and 0.7R has greater dispersion. Figure 13 shows the dimensionless processing results with the inner parameters. The high-band normalization at 0.9R radius has a better effect, while the dispersion of other radii is larger. The turbulent boundary layer flow state of the propeller blade surface is complicated, with strong pressure gradient changes, and there may be flow separation at the trailing edge of the blade, which will affect the generation of turbulent pulsating pressure. However, simply processing the characteristic quantities with inner and outer parameters of the boundary layer may not be enough to reflect the factors affected by the pulsating pressure. However, the turbulent pulsating pressure on the blade surface is an important source for generating flow-induced noise, and the accurate simulation of its characteristics is an important basis for predicting the far-field acoustic radiation of the propeller.

4.4 Radiation Noise Characteristics

The noise monitoring point is located on the side of the propeller, 0.7m away from the propeller shaft (Figure 5). The noise monitoring point is consistent with the test state. The flow velocity is 4m/s and the rotation speed is 30rps. Figure 14 shows the vortex structure on the blade surface, and the boundary between laminar flow and turbulent flow regions can be clearly seen. There is a large laminar flow region in the inner radius, while most of the outer radius is a turbulent region. Figure 15 shows the vortex structure on the blade surface at 0.7R section. Most of the vortex structures are close to the blade surface, while the external flow field area away from the object surface has fewer vortex structures. The comparison between the calculated results of propeller noise and the test results is shown in Figure 16. It can be seen that the test results decrease before 2k Hz and rise after 2k Hz, and the simulation results can basically reflect this trend. The calculated result is lower than the test result before 0.8k Hz, mainly because the signal quantity of low frequency noise is too large due to the influence of low frequency vibration and other factors of test equipment. Compared with the experimental results, the error of the calculated results in the frequency range above 1.25 kHz is about ~5dB. Two sets of cells are used in the simulation results, with a fine cell number of 45 million and a coarse cell number of 22.5 million. It can be seen that cell refinement has little impact on the spectrum before 1.25 kHz. At 1.6 kHz and 2 kHz, the amplitude of the fine cell is higher than that of the coarse cell, but at the frequency band higher than 2.5 kHz, the coarse cell is higher than the dense cell. Figure 17 shows the comparison between propeller thickness noise and loading noise. Propeller thickness noise is mainly generated by the spatial inhomogeneity caused by propeller rotation, which mainly affects low frequency noise, but has little influence on middle and high frequency noise. The propeller loading noise is mainly caused by the turbulent pulsation pressure on the blade surface. The turbulent structure captured by the refinement mesh is smaller, and the turbulent pulsation frequency stimulated by the small turbulent structure is higher, so the amplitude of the noise spectrum is higher. However, the simulation results in this paper are only reflected in the 1.6 kHz and 2 kHz frequency bands. In the higher frequency bands, the amplitude obtained by the dense cell decreases, which indicates that the noise in the higher frequency bands is more likely to be pseudo-noise rather than noise signals generated by real turbulence.

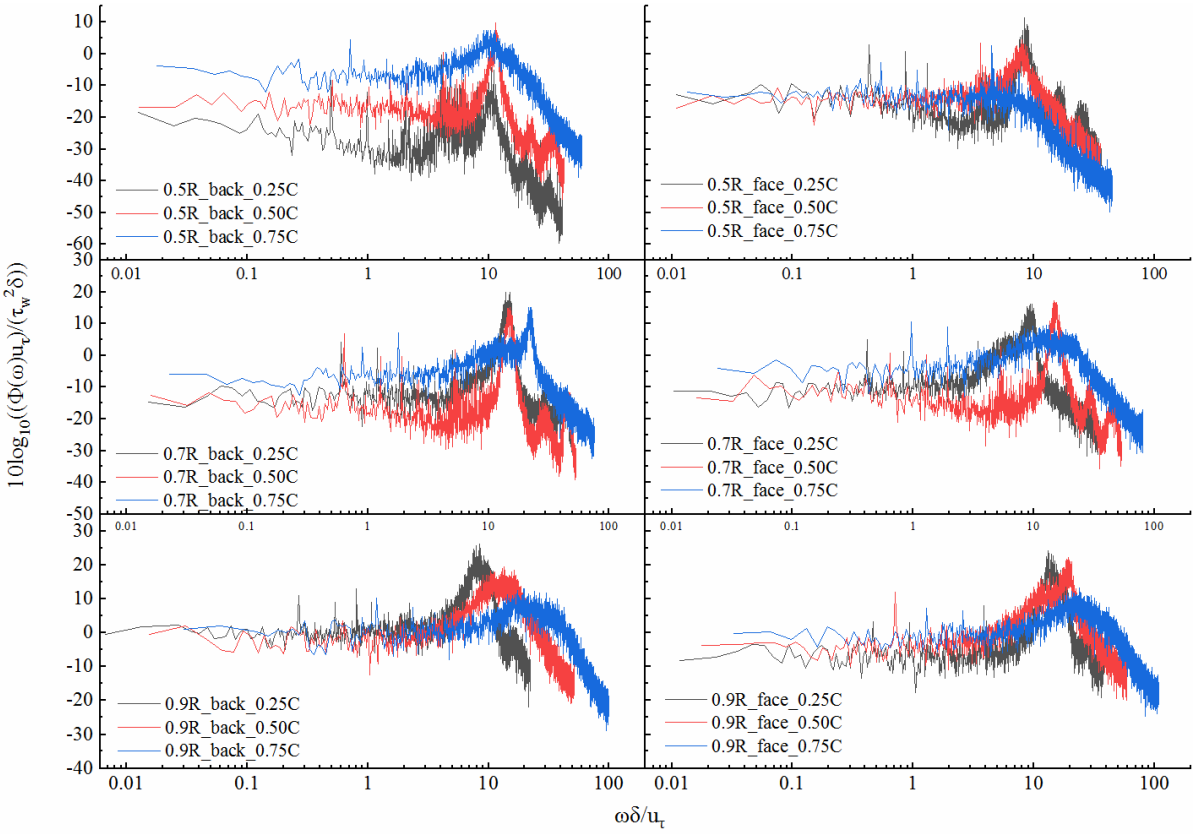

Figure 12 The spectral diagram of pulsating pressure is dimensionless by using the outer boundary layer parameters

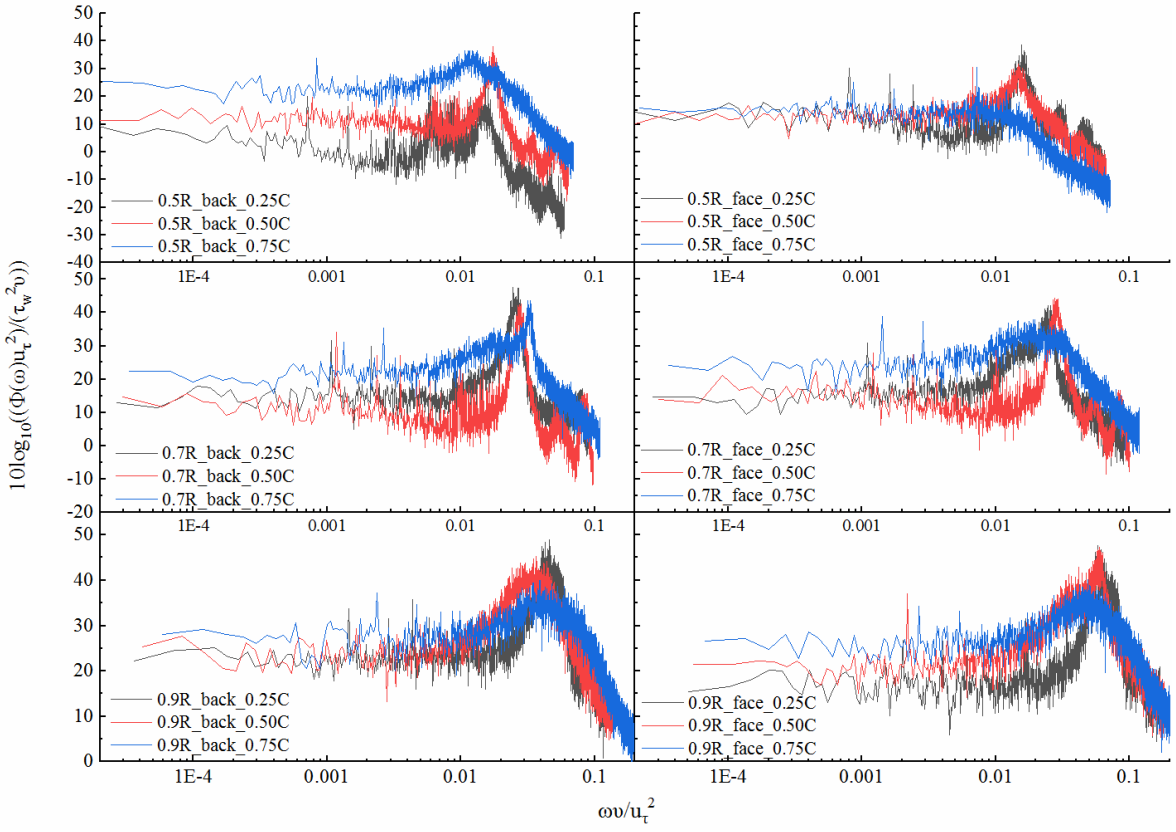

Figure 13 The spectral diagram of pulsating pressure is dimensionless with the parameters of the inner boundary layer

In order to better analyze the contribution of different radius regions of the propeller to the noise, the propeller is divided into different noise sources according to different radii, as shown in Figure 18. The noise results of each part are calculated in the same calculation condition as shown in Figure 19. It can be seen that the noise amplitude of the outer radius is higher than that of the inner radius, which is mainly due to the higher incoming flow velocity of the

outer radius, and its local Reynolds number is higher than that of the inner radius. Similarly, the pulsating pressure excitation in the outer radius is higher, as shown in Figure 11. So extra attention needs to be paid to the outer radius blade shape parameter when designing the propeller to control the propeller noise level.

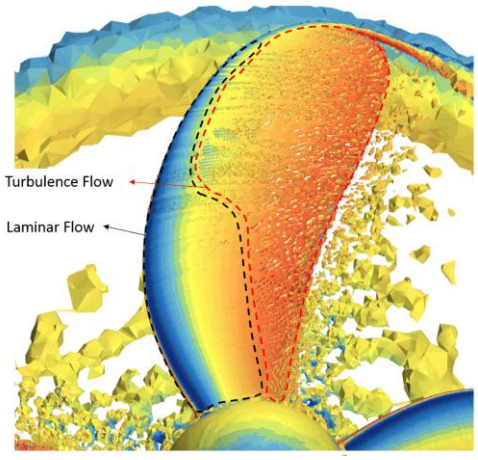

Figure 14 The vortex structure on the blade, Q=1000 1/s^2

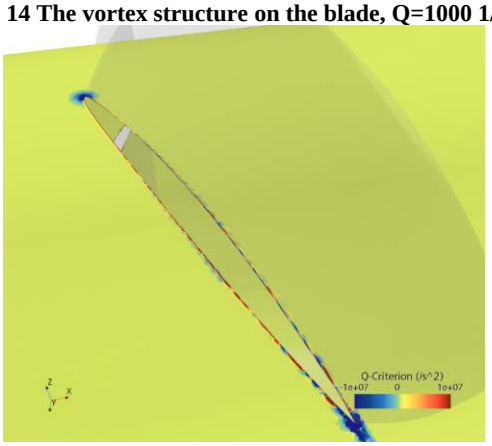

Figure 15 The vortex structure around the blade, expressed by Q criterion (0.7R)

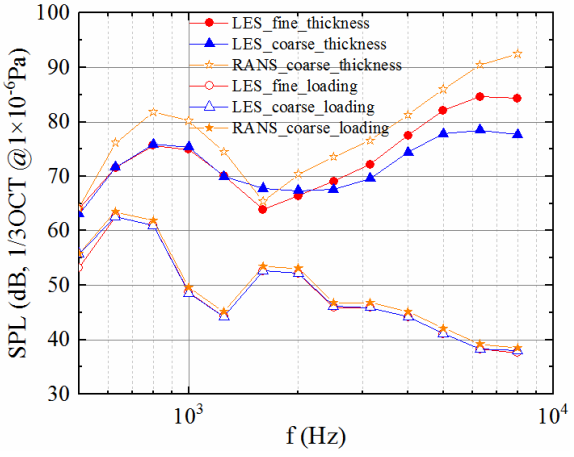

Figure 16 The calculation results of propeller noise compared with the experimental results

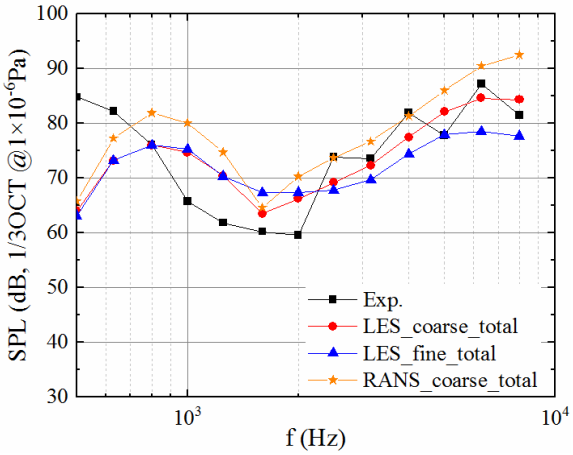

Figure 17 Comparison of propeller noise thickness noise and loading noise

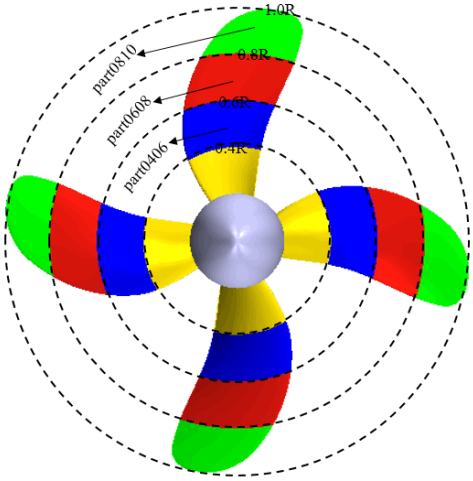

Figure 18 Schematic diagram of the division of the sound source area of the propeller

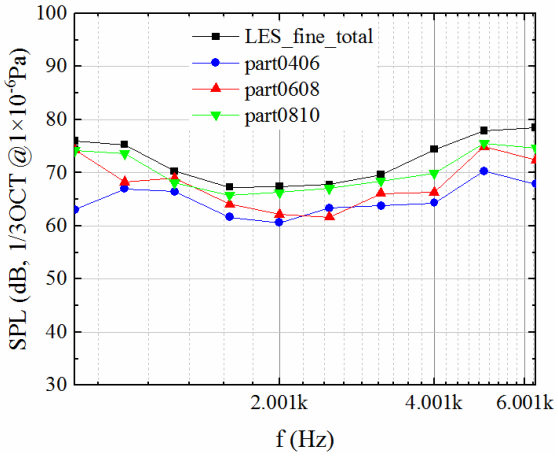

Figure 19 Comparison of propeller noise thickness noise and loading noise

5 CONCLUTIONS

In this paper, the large eddy simulation method is used to obtain the flow field around the propeller, then the propeller noise is predicted based on acoustic analogy method. The characteristics of propeller noise in middle and high frequency bands are mainly studied. By studying the characteristics of turbulent boundary layer and pulsating pressure of propeller, the main distribution

characteristics of noise excitation source on blade surface are obtained. The main conclusions are as follows:

1) The flow and pulsating pressure excitation sources of the boundary layer on the blade surface are obtained by the numerical simulation method, and the hydrodynamic noise characteristics of the propeller can be predicted by the acoustic analogy method.

2) In the model scale, a thin boundary layer flow is formed on the surface of the propeller blade. Due to the profile shape of the blade, the pressure distribution in most regions is a non-zero pressure gradient, so the pressure pulsation is relatively complex. A unified normalization result can be obtained by using the inner or outer parameters of the boundary layer at the radius of 0.9R, while it is difficult to obtain at other radii.

3) The noise results of the propeller are obtained by acoustic analogy method and compared with the experimental results. The deviation of the predictions above 1.25 kHz is about ~5dB.

4) The noise source character shows that the outer radius of the blade generates higher noise amplitude than the inner radius, and a similar pattern is observed in wall fluctuating pressure on the blade surface.

The model propeller has a high Reynolds number of the blade surface flow and a thinner turbulent boundary layer, which puts forward higher requirements for numerical simulation. In the future, a more detailed study on the flow structure characteristics of the blade surface is needed to improve the prediction accuracy of middle and high frequency noise.

REFERENCES

Bensow, R. E. & Liefvendahl, M. (2016). 'An acoustic analogy and scale-resolving flow simulation methodology for the prediction of propeller radiated noise'. 31st Symposium on Naval Hydrodynamics. Monterey, USA.

Bogey, C., Bailly, C. (2004). 'A family of low dispersive and low dissipative explicit schemes for flow and noise computations'. Journal of Computational Physics, 194(1): 194-214.

Brentner, K. S. & Farassat, F. (1998). 'Analytical Comparison of the Acoustic Analogy and Kirchoff Formulation for Moving Surfaces'. AIAA Journal, Vol. 36, No.8, 1379-1386.

Cianferra, M., Petronio, A., Armenio, V. (2019). 'Numerical prediction of ship propeller noise through acoustic analogy'. Sixth International Symposium on Marine Propulsors smp'09, Rome, Italy.

Clauser, F. H. (1954). 'Turbulent boundary layer in adverse pressure gradients'. J. Aeronaut. Sci., 21 (2), 91–108.

Curle, N. (1955). 'The Influence of Solid Boundaries On Aerodynamic Sound'. Proc. Roy. London Soc., 231A, 1187, 505-514.

Ffowcs Williams, J. E. & Hawkings, D. L. (1969). 'Sound Generated by Turbulence and Surfaces in Arbitrary Motion'. Philosophical Transactions of the Royal Society, Vol. A264, N0.1151, 321-342.

Francescantonio, P. D. (1997). 'A new boundary integral formulation for the prediction of sound radiation'. Journal of Sound & Vibration, 202(4), 491-509.

Farabee, T. M. & Casarella, M. J. (1991). 'Spectral features of wall pressure fluctuations beneath turbulent boundary layers.' Phys. Fluids, A 3, 2410–2420.

Hallander, J., Lee, D. Q., Allenstrom, B., Valdenazzi, F., & Barras, C. (2012). 'Predicting Underwater Radiated Noise due to a Cavitating Propeller in a Ship Wake'. International Symposium on Cavitation - CAV2012, Singapore.

Ianniello, S., Muscari, R. & Mascio, A. D. (2013). 'Ship underwater noise assessment by the acoustic analogy. part i: nonlinear analysis of a marine propeller in a uniform flow'. Journal of Marine Science & Technology, 18, 547–570.

Jang, J. S., Kim, H. T., & Joo, W. H. (2015). 'Numerical Study on Non-Cavitating Noise of Marine Propeller'. International Congress and Exposition on Noise Control Engineering, Melbourne, Australia.

Jarrin, N., Benamadouche, S., Laurence, D. and Prosser, R. (2006). 'A synthetic-eddy-method for generating inflow conditions for large eddy simulations'. International Journal of Heat and Fluid Flow, 27, 585-593.

Lidtke, A. K., Humphrey, V. F. & Turnock, S. R. (2016). 'Feasibility study into a computational approach for marine propeller noise and cavitation modelling'. Ocean Engineering, 120(1), 152-159.

Lighthill, M. J. (1952). 'On Sound Generated Aerodynamically. I. General Theory'. Proc. Roy.London Soc., 211A, 1107, 564-587.

Lloyd, T. P., Rijpkema, D. & Wijngaarden, E. V. (2014). 'Implementing the Ffowcs Williams-Hawkings acoustic analogy into a viscous CFD solver'. Numerical Towing Tank Symposium. Marstrand, Sweden.

Magionesi, F. & Di Mascio, A. (2016). 'Investigation and modelling of the turbulent wall pressure fluctuations on the bulbous bow of a ship'. Journal of Fluids and Structures, 67, 219-240.

Nicoud, F. & Ducros, F. (1999). 'Subgrid-Scale Stress Modelling Based on the Square of the Velocity Gradient Tensor'. Flow, Turbulence and Combustion, 62, 183-200.

Nitzkorski, Z. L. (2015). 'A novel porous ffowcs-williams and hawkings acoustic methodology for complex geometries'. Ph.D. Thesis, 2-7.

Seol, H., Jung, B., Suh, J. C. & Lee, S. (2002). 'Prediction of non-cavitating underwater propeller noise'. Journal of Sound & Vibration, 257(1), 131-156.